The Astrophysical Journal, 752:48 (10pp), 2012 June 10 doi:10.1088/0004-637X/752/1/48

DYNAMICS OF THE SOLAR MAGNETIC BRIGHT POINTS DERIVED FROM THEIR HORIZONTAL MOTIONS

L. P. Chitta[1,2], A. A. van Ballegooijen[1], L. Rouppe van der Voort[3], E. E. DeLuca[1], and R. Kariyappa[2]
[1] Harvard-Smithsonian Center for Astrophysics, 60 Garden Street MS-15, Cambridge, MA 02138, USA
[2] Indian Institute of Astrophysics, Bangalore 560 034, India
[3] Institute of Theoretical Astrophysics, University of Oslo, P.O. Box 1029, Blindern, NO-0315 Oslo, Norway
Received 2012 March 7; accepted 2012 April 10; published 2012 May 24

ABSTRACT

The subarcsecond bright points (BPs) associated with the small-scale magnetic fields in the lower solar atmosphere are advected by the evolution of the photospheric granules. We measure various quantities related to the horizontal motions of the BPs observed in two wavelengths, including the velocity autocorrelation function. A 1 hr time sequence of wideband Hα observations conducted at the Swedish 1 m Solar Telescope (SST) and a 4 hr *Hinode* *G*-band time sequence observed with the Solar Optical Telescope are used in this work. We follow 97 SST and 212 *Hinode* BPs with 3800 and 1950 individual velocity measurements, respectively. For its high cadence of 5 s as compared to 30 s for *Hinode* data, we emphasize more the results from SST data. The BP positional uncertainty achieved by SST is as low as 3 km. The position errors contribute 0.75 km^2 s^{-2} to the variance of the observed velocities. The *raw* and *corrected* velocity measurements in both directions, i.e., (v_x, v_y), have Gaussian distributions with standard deviations of (1.32, 1.22) and (1.00, 0.86) km s^{-1}, respectively. The BP motions have correlation times of about 22–30 s. We construct the power spectrum of the horizontal motions as a function of frequency, a quantity that is useful and relevant to the studies of generation of Alfvén waves. Photospheric turbulent diffusion at timescales less than 200 s is found to satisfy a power law with an index of 1.59.

Key words: Sun: photosphere – Sun: surface magnetism

Online-only material: animation, color figures

1. INTRODUCTION

The discrete and small-scale component of the solar magnetic field is revealed in the high spatial resolution observations of the Sun. Ground-based observations (Muller 1983, 1985; Berger et al. 1995) show clusters or a network of many bright points (hereafter BPs) in the intergranular lanes, with each individual BP having a typical size of 100–150 km. These BPs are known to be kilogauss flux tubes in the small-scale magnetic field (SMF), and are extensively used as proxies for such flux tubes (Chapman & Sheeley 1968; Stenflo 1973; Stenflo & Harvey 1985; Title et al. 1987; see de Wijn et al. 2009 for a review on the SMF). High-cadence observations and studies show that magnetic BPs are highly dynamic and intermittent in nature, randomly moving in the dark intergranular lanes.[4] These motions are mainly due to the buffeting of granules. The SMF is passively advected to the boundaries of supergranules creating the magnetic network in the photosphere.

Earlier works by several authors have reported mean rms velocities of magnetic elements in the order of a few km s^{-1}. With the ground-based observations of the granules at 5750 Å (white light), Muller et al. (1994) have identified many network BPs with turbulent proper motion and a mean speed of 1.4 km s^{-1}. Berger & Title (1996) have used *G*-band observations of the photosphere and found that the *G*-band BPs move in the intergranular lanes at speeds from 0.5 to 5 km s^{-1}. Berger et al. (1998) observed the flowfield properties of the photosphere by comparing the magnetic network and nonmagnetic quiet Sun. They show that the convective flow structures are smaller and much more chaotic in the magnetic region, with a mean speed of 1.47 km s^{-1} for the tracked magnetic BPs. With the *G*-band and continuum filtergrams, van Ballegooijen et al. (1998) used an object tracking technique and determined the autocorrelation function describing the temporal variation of the bright point velocity, with a correlation time of about 100 s. Correcting for measurements errors, Nisenson et al. (2003) measured a 0.89 km s^{-1} rms velocity for BPs. Advances in ground-based observations like rapid high-cadence sequences with improved adaptive optics (AO) to minimize seeing effects, and also space-based observations at high resolutions, continued to attract many authors to pursue BP motion studies. For example, Utz et al. (2010) used space-based *Hinode* *G*-band images to measure BP velocities and their lifetimes. The BP motions can be used to measure dynamic properties of magnetic flux tubes and their interaction with granular plasma. Photospheric turbulent diffusion is one such dynamical aspect that can be derived consequently from the BP random walk. Manso Sainz et al. (2011) measured a diffusion constant of 195 km^2 s^{-1} from the BP random walk and their dispersion. Abramenko et al. (2011) studied photospheric diffusion at a cadence of 10 s with high-resolution TiO observations of a quiet-Sun area. They found a super-diffusion regime, satisfying a power law of diffusion with an index $\gamma = 1.53$, which is pronounced in the time intervals 10–300 s.

The implications of these magnetic random walk motions have recently been found to be very fruitful. Such motions are capable of launching magnetohydrodynamic (MHD) waves (Spruit 1981), which are potential candidates for explaining the high temperatures observed in the solar chromosphere and corona. For example, a three-dimensional MHD model developed by van Ballegooijen et al. (2011) suggests that random motions inside BPs can create Alfvén wave turbulence, which dissipates the waves in a coronal loop (also see Asgari-Targhi & van Ballegooijen 2012). Observations by De Pontieu et al. (2007b), Jess et al. (2009), and McIntosh et al. (2011)

[4] See an accompanying animation of SST data used in this study. Also see TiO animations at http://www.bbso.njit.edu/nst_gallery.html, and *G*-band animations at http://solar-b.nao.ac.jp/QLmovies/index_e.shtml.

provide strong evidence that the Alfvénic waves (which are probably generated by the BP motions) have sufficient energy to heat the quiet solar corona. To test theories of chromospheric and coronal heating, more precise measurements of the velocities and power spectra of BP motions are needed.

Nisenson et al. (2003) worked on the precise measurements of BP positions, taking into account the measurement errors. The autocorrelations derived by them for the *x*- and *y*-components of BP velocity using high spatial resolution and moderate cadence of 30 s observations gave a correlation time of about 60 s, which is twice the cadence of the observations. This suggests an overestimation of correlation time and an underestimation of the rms velocity power, with significant hidden power in timescales less than 30 s, and thus warranting observations at even higher cadence. This is important because the measured power profile, which is the Fourier transform of the autocorrelation function, gives us an estimate of the velocity amplitudes and energy flux carried by the waves that are generated by the BP motions in various, and especially at, higher frequencies.

In this study, we use 5 s cadence wideband Hα observations from the Swedish 1 m Solar Telescope (SST) to track the BPs and measure their rms velocities. For comparison, we also use a 30 s cadence *G*-band observational sequence from the Solar Optical Telescope (SOT) on board *Hinode*. These independent and complementary results take us closer to what could be the true rms velocity and power profile of the lateral motions of the BPs. The details of the data sets used, analysis procedure, results, and their implications are discussed in the following sections.

2. DATA SETS

In this study, we have analyzed time sequences of intensity filtergrams with 5 and 30 s cadence. A brief description of the observations is given below.

5 s data. These observations were obtained on 2006 June 18, with the SST (Scharmer et al. 2003a) on La Palma, using the AO system (Scharmer et al. 2003b) in combination with the Multi-Object Multi-Frame Blind Deconvolution (MOMFBD; van Noort et al. 2005) image restoration method under excellent seeing conditions. The target area is a quiet-Sun region away from disk center at $(x, y) = (-307,'' -54'')$ and $\mu = 0.94$ (see Figure 1). The time sequence is of one hour duration starting at 13:10 UT. Here we analyze images from the wideband channel of the Solar Optical Universal Polarimeter (SOUP; Title & Rosenberg 1981) which received 10% of the light before the SOUP tunable filter but after the SOUP prefilter (see De Pontieu et al. 2007a for the optical setup of the instrument). The prefilter was an FWHM = 8 Å wide interference filter centered on the Hα line. The SOUP filter was tuned to the blue wing of Hα at −450 mÅ but those data are not considered here. On the wideband channel, there were two cameras (running at 37 frames per second) positioned as a phase-diversity pair—one in focus and one camera 13.5 mm out of focus. The data from the two cameras have been processed with the MOMFBD restoration method in sets of 5 s, creating a 5 s cadence time sequence with a total of 720 images. After MOMFBD processing, the restored images were de-rotated to account for the field rotation due to the altazimuth mount of the telescope. Furthermore, the images were aligned using cross-correlation on a large area of the field of view (FOV). The images were then clipped to 833×821 pixels (with $0\farcs065$ pixel^{-1}), to keep the common FOV (the CCDs have 1024×1024 pixels, some pixels are lost after alignment between focus and defocus cameras).

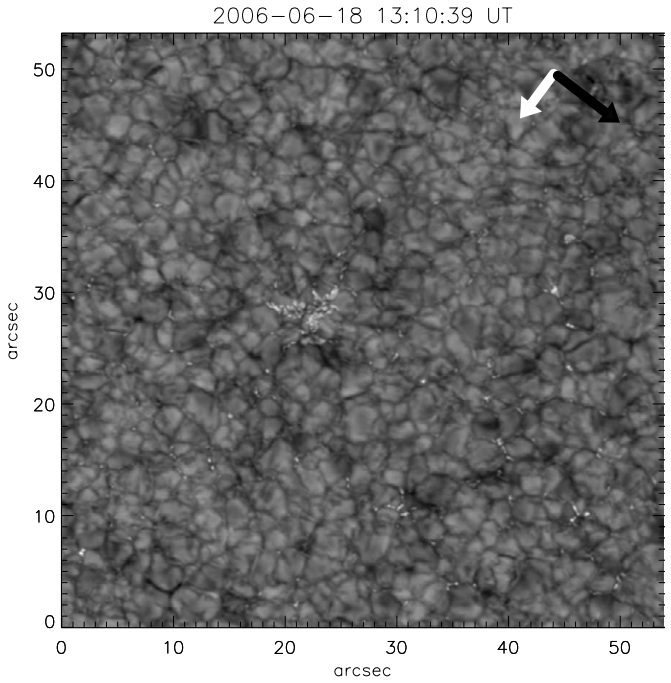

Figure 1. First image from the time sequence of SST wideband Hα observations at 13:10 UT on 2006 June 18. The black arrow is pointing toward solar north and the white arrow is toward disk center.

(An animation of this figure is available in the online journal.)

For a reference direction, the solar north in the SST time sequence is found by aligning an earlier SST observation of that day of an active region (AR) magnetogram to a full disk *Solar and Heliospheric Observatory*/MDI magnetogram (the AR was just outside the MDI high-resolution region). From that comparison, we fix the direction of the solar north and disk center (black and white arrows, respectively, in Figure 1). Though we do not rotate the images to match the solar north during our analysis, the angles are taken into account at a later stage to correct for projection effects in the velocity measurements.

30 s data. We use *G*-band filtergrams observed with the SOT on board *Hinode* (Kosugi et al. 2007; Tsuneta et al. 2008) on 2007 April 14. The observations were made for a duration of 4 hr, with a 30 s cadence in an FOV of $55'' \times 55''$ ($0\farcs05$ pixel^{-1}; 1024 pixels in both the *x*- and *y*-directions), near disk center. The images were processed using standard procedures available in the *solarsoft* library.

3. PROCEDURE

In this section, we briefly describe the method of determining the BP positions, and the velocity measurements through the correlation tracking.

3.1. BP Positions

We manually select the BPs to estimate their position to a sub-pixel accuracy. We consider the coordinates of maximum intensity of a given BP to be the position of that BP, and the method for measuring these positions involves two steps. In the first step, we visually identify a BP and it is selected for analysis for a period during which it is clearly distinguishable from the surrounding granules. On average, we follow a BP for about 3–5 minutes. The BPs with elongated shapes are not considered for analysis. Also, we stop following a BP if

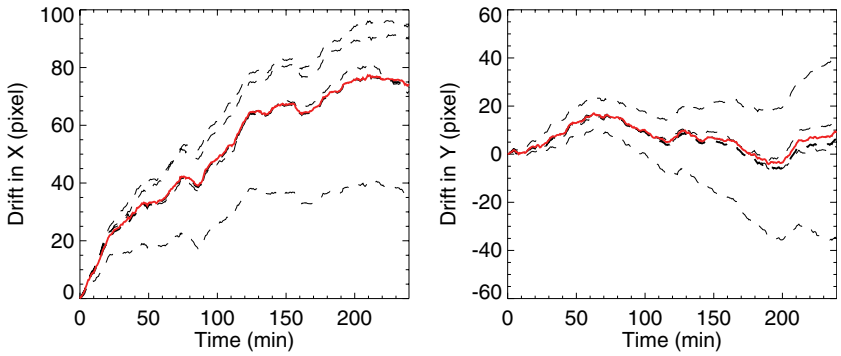

Figure 2. Illustration of different offsets seen in the full and partial FOV of *Hinode* data. Dashed curves in the left (right) panel show the drifts in the *x*- (*y*-) direction of the four selected quadrants. Thick dashed profile is the average of four dashed curves. Thick red profile is the drift of the full FOV (see the text for details).
(A color version of this figure is available in the online journal.)

it is substantially distorted or elongated from its initial shape. Though time consuming, manual selection gives a handle on the validity of the positional accuracy of a BP from frame to frame. At each time step, using a cursor, an approximate location $(x'_{\rm app}, y'_{\rm app})$ of a particular BP is fed to an automated procedure to get its accurate position, which is step two in our method.

Step two is completely an automated procedure. Here, we use a surface interpolation technique to get a precise position of that BP (to a sub-pixel accuracy). The approximate position from the previous step is used to construct a grid of 5×5 pixels covering the full BP (with $(x'_{\rm app}, y'_{\rm app})$ as the center of that grid). Now, our procedure fits a two-dimensional, fourth-degree surface polynomial to that grid (using *SFIT*, an IDL procedure); interpolates the fit to one-hundredth of a pixel; returns the fine location of its peak $(\delta x', \delta y')$ within that grid; and finally stores the accurate position $(x'_{\rm BP}, y'_{\rm BP})$ of that BP (which is the sum of its approximate and fine positions $(x'_{\rm app} + \delta x', y'_{\rm app} + \delta y')$), for further analysis. Therefore, the position of a BP with index j in a frame i is given by

$$(x'_{\rm BP}, y'_{\rm BP})^j_i = (x'_{\rm app} + \delta x', y'_{\rm app} + \delta y')^j_i, \quad (1)$$

and all the coordinates until this point are relative to the lower left corner of the image.

3.2. Reference Frame

Though the positional measurements of BPs as described in Section 3.1 are accurate, they cannot be directly used to measure the velocities as there are artificial velocity sources, viz., instrumental drifts, seeing variations, jittery motions, and also solar rotation, which vectorially add to BP velocities and thus are required to be removed from the analysis. While *Hinode* (space-based) data are not subjected to seeing variations, SST (ground-based) data have been corrected for seeing as described in Section 2. Further, we need to correct for instrumental drifts, jitters, and solar rotation. Calculating the offsets between successive images is necessary to remove these artificial velocities. In this section, we describe the method of our cross-correlation analysis used to co-align the images.

Cross-correlation (C) of two images $f(x, y)$ and $g(x, y)$ is defined as

$$C = \frac{1}{k-1} \sum_{x,y} \frac{(f(x, y) - \overline{f})(g(x, y) - \overline{g})}{\sigma_f \sigma_g}, \quad (2)$$

where, $\overline{f}$ $[\overline{g}]$ and σ_f $[\sigma_g]$ are the mean value and standard deviation of $f(x, y)$ $[g(x, y)]$, respectively, and k is the number of pixels in each image, for normalization. With the above definition of cross-correlation, to get the offsets between two images, we need to shift one image with respect to the other (in both the *x*- and *y*-directions) and find at what offsets (independent in *x* and *y*) the correlation function attains the maximum value. In general, for shifts of $-l$ to $+l$, the cross-correlation is a two-dimensional function with $2l + 1$ rows and columns. Let l_x and l_y be the coarse offsets between the two images in the *x*- and *y*-directions, respectively, such that the cross-correlation reaches its maximum value: $\max(C) = C(l_x, l_y)$, where $-l < l_x, l_y < l$. To get the sub-pixel offsets, the fine offsets $(\delta l_x, \delta l_y)$ are calculated. The method is similar to finding the fine position of BP by using a 5×5 pixel grid but now about the (l_x, l_y) of C.

Instead of cross-correlating every successive image with its previous one, we keep a reference image for about 200 s, i.e., a frame i taken at time t (i_t) is used as a reference for the subsequent frames until $t + 200$ s (i_{t+200}) for cross-correlation. Therefore, the *5 s* (SST) and the *30 s* (*Hinode*) data have about 40 and 7 images, respectively, in each set. By keeping the last image of a set equal to the first image in its next set, we can co-align different sets. In this way, the accumulation of errors in the offsets can be minimized.

Using the above background on co-aligning images to find various drifts, we present the results of drifts found in *Hinode* data. As an illustration, we divide the full (i.e., $55'' \times 55'' \times 4$ hr) *Hinode* time sequence into four quadrants with $27\farcs5 \times 27\farcs5 \times 4$ hr each. Further, we perform correlation tracking (as described above by keeping seven frames per set) on each quadrant separately and plot the results in Figure 2. The four dashed lines in the left and the right panels are the offsets in the *x*- and *y*-directions, respectively, the thick dashed line in each panel is the average of the offsets (i.e., average of four dashed lines), and the solid red curve is the offset obtained by considering the full FOV. Clearly, in each quadrant, the offsets have a trend similar to that of the full FOV (solid red curve) and an additional component of their own. This additional component is probably the real velocity on the Sun due to flows with varying length scales (for example, supergranular, meso-granular, and granular) and with flow directions changing over areas of a few tens of arcsec^2 on the Sun.

In this paper we are mainly interested in the dynamics of the BPs relative to their *local* surroundings, as granulation flows will have a dominant effect on the BP velocities and their variations on short timescales. Hence, we consider a $5'' \times 5''$ area about the BP as a reference frame for that BP (i.e., keeping the BP in the center of the *local* area). The cross-correlation is performed on this $5'' \times 5''$ area instead of on the full FOV to

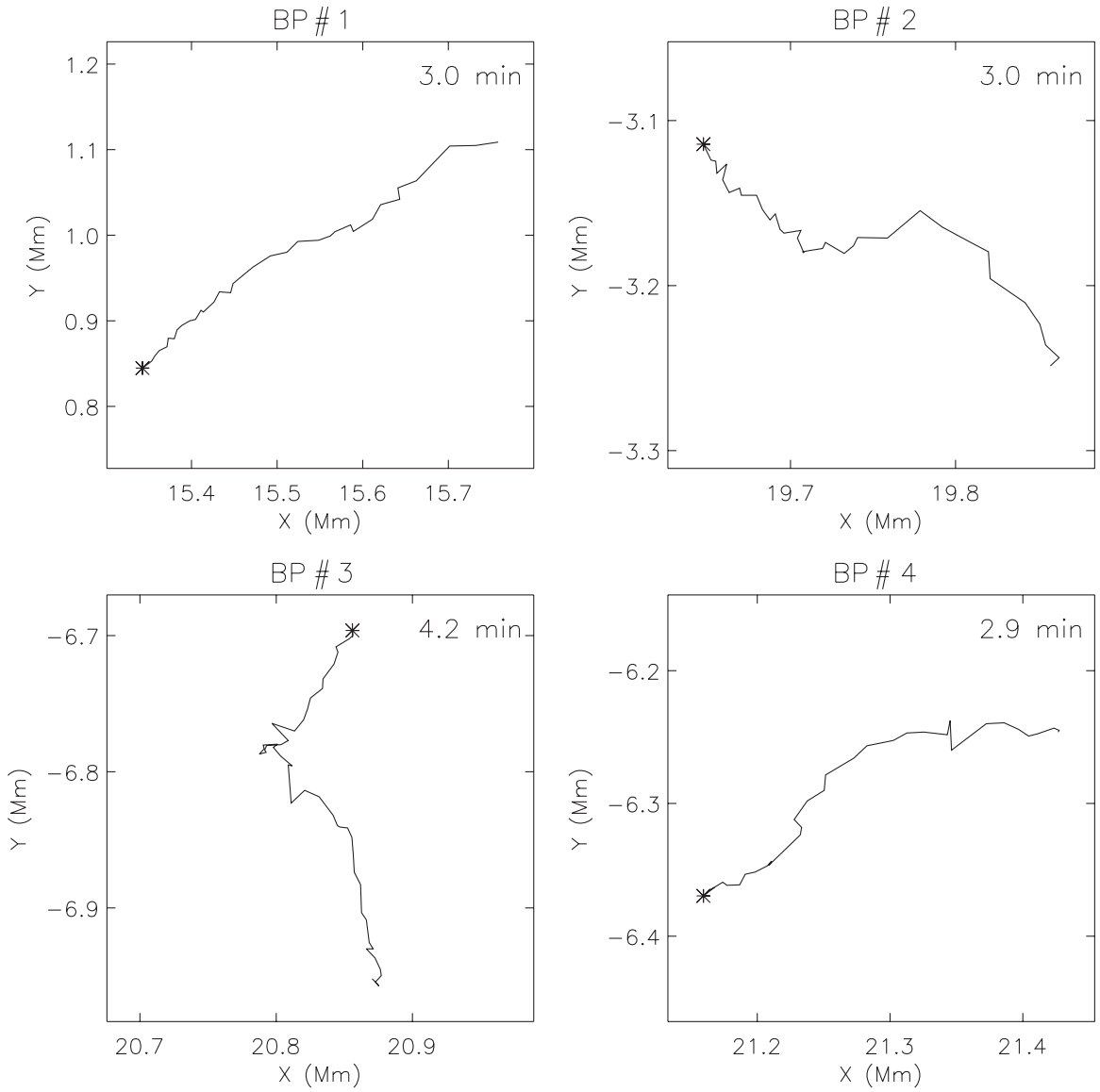

Figure 3. Examples of the paths of four BPs taken from the SST data. The initial position of each BP is marked with a star. Time shown at the top right corner in each panel is the duration for which respective BP is followed.

get the offsets, which are subtracted from $(x'_{\rm BP}, y'_{\rm BP})^j_i$. The BP positions corrected for offsets are now given by

$$(x'_{\rm BPC}, y'_{\rm BPC})^j_i = (x'_{\rm BP}, y'_{\rm BP})^j_i - (l_x + \delta l_x, l_y + \delta l_y)^{j_{\rm local}}_i, \quad (3)$$

where $j_{\rm local}$ represents the *local* area of BP^j.

In the case of SST data, the observations are off disk center at $(-307'', -54'')$, which corresponds to a heliocentric angle of arccos(0.94). This will introduce a projection effect on the measured horizontal velocities in both the x'- and y'-directions and needs to be corrected. To do this, the coordinate system (x', y') defined by the original SST observations is rotated by 45° in the anticlockwise direction. Now the image plane is oriented in the E–W (parallel to equator, new x-) and N–S (new y-) directions. Further, the E–W coordinate is multiplied by a factor of 0.94^{-1}. Hence, the new coordinate system (x, y) is given by

$$x = (x' \cos 45^\circ + y' \sin 45^\circ) \times \frac{1}{0.94},$$
$$y = (-x' \sin 45^\circ + y' \cos 45^\circ). \quad (4)$$

The SST BP positions $(x'_{\rm BPC}, y'_{\rm BPC})^j_i$, as measured from Equation (3), are remapped to $(x_{\rm BPC}, x_{\rm BPC})^j_i$, using the above coordinate transformations.[5]

4. RESULTS

In this section, we present various results in detail giving more emphasis on the SST results. We have selected 97 SST BPs with ∼3800 individual velocity measurements.[6] Figure 3 shows the paths of four individual SST BPs. Some of the BPs move in a relatively smoother path while some exhibit very random motions to the shortest time steps available. BPs drift about a few hundred km in a few minutes. The instantaneous velocity $(v_x, v_y)^j_{i+1}$ of a BP is given by $(x_{\rm BPC}, y_{\rm BPC})^j_{i+1} - (x_{\rm BPC}, y_{\rm BPC})^j_i$, multiplied by a factor to convert the units of measured velocity to km s^{-1}

[5] Note that the transformations in Equation (4) are only to modify the SST BP positions, and in the rest of the paper, we use (x, y) for the remapped (x', y') of SST and (x, y) of *Hinode*.

[6] Similarly, we have identified 212 *Hinode* BPs with 1950 individual velocity measurements.

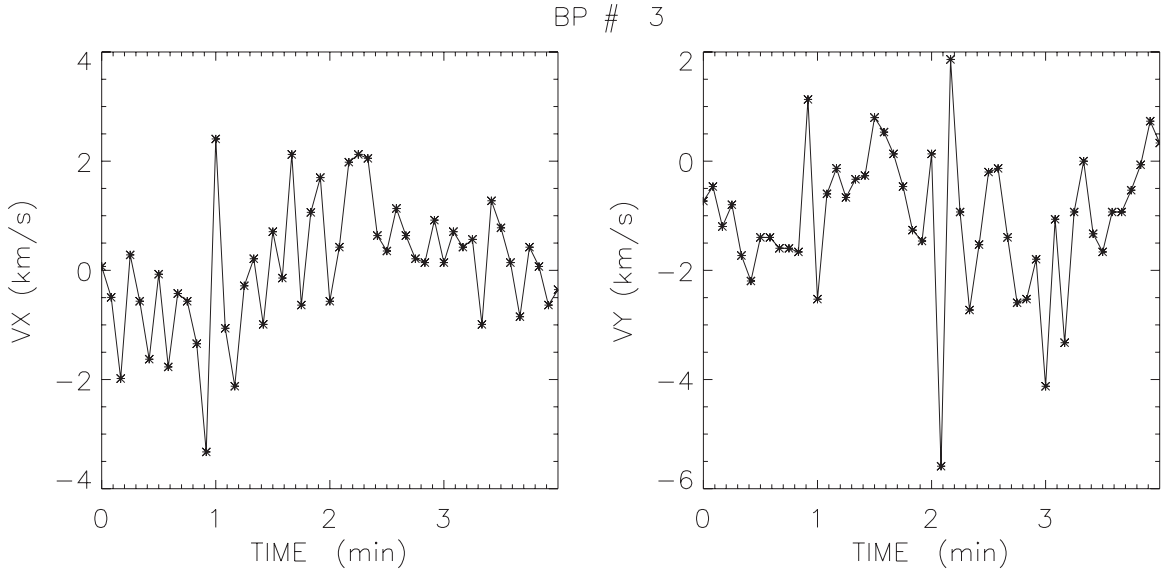

Figure 4. Velocities v_x and v_y as a function of time for a typical BP (shown here for BP#3; see Figure 3 for the track of BP#3).

Table 1
Properties of the Velocity Distributions in Figure 5

	v_x (km s^{-1})		v_y (km s^{-1})	
	$\langle v_x \rangle$	$\sigma(v_x)$	$\langle v_y \rangle$	$\sigma(v_y)$
Histogram	0.18	1.58	0.19	1.54
Gaussian fit ($\sigma_{v,r}$)	0.01	1.32	0.01	1.22
Corrected distribution ($\sigma_{v,c}$)	0.01	1.00	0.01	0.86

(9.4 in the case of SST which is the image scale of SST in kilometers divided by the time cadence in seconds). Figure 4 shows the plot of such velocities as a function of time for BP#3 (path of BP#3 is shown in the lower left panel of Figure 3). Usually, the changes in the velocity are gradual in time but, sometimes, we do see sudden and large changes in the magnitude and direction of the velocity (for example, at 1 minute in v_x and at 2 minutes in v_y in Figure 4). Note that a large change of velocity of one sign is followed immediately by a change of the opposite sign, so the net change in position is not very large. This suggest that these changes are due to errors in the positional measurements. A position error at one time will affect the velocities in the intervals immediately before and after that time. In the following we will assume that such changes in velocity are due to measurement errors. However, we cannot rule out that some of these changes are due to real motions on the Sun on timescales less than 5 s.

The means and standard deviations of v_x and v_y are listed in Table 1 (first line). Histograms of the distribution of velocities v_x, v_y, and $v = \sqrt{v_x^2 + v_y^2}$ are shown in Figure 5 (panels (a), (b), and (c), respectively). Solid lines in panels (a) and (b) are Gaussian fits to the histograms with *raw* standard deviations ($\sigma_{v,r}$) of 1.32 and 1.22 km s^{-1}. A scatter plot of v_x against v_y is shown in panel (d), which is symmetric in the v-space. However, a small non-zero and positive mean velocity of about 0.2 km s^{-1} is noticed, suggesting that there is a net BP velocity with respect to the 5 arcsec boxes that we used as reference frames. Values of the mean and rms velocities as determined from the fits are also listed in Table 1 (second line). These distributions are a mix of both true velocities and measurement errors.

We can gain more insight into the dynamical aspects of the BP motions by studying their observed velocity correlation function $c(t)$, defined as

$$c_{xx,n} = \langle v_{x,i}^j v_{x,i+n}^j \rangle, \quad c_{yy,n} = \langle v_{y,i}^j v_{y,i+n}^j \rangle \tag{5}$$

$$c_{xy,n} = \langle v_{x,i}^j v_{y,i+n}^j \rangle, \tag{6}$$

where $c_{xx,n}$, $c_{yy,n}$ are the autocorrelations, $c_{xy,n}$ is the cross-correlation of v_x and v_y, and n is the index of the delay time. $\langle \cdots \rangle$ denotes the average over all values of the time index i and BP index j but for a fixed value of n. These results are shown in Figure 6. Top left and right panels are the plots of c_{xx} and c_{yy}, respectively. Black curves are for the SST, whereas the red curves show the *Hinode* results for comparison. Both the SST and *Hinode* results are consistent for delay times <1 minute. However, the *Hinode* autocorrelations quickly fall to lower values. This is mainly a statistical error, since we do not have a large number of measurements in the case of *Hinode*. Focusing on periods <1 minute, it is clear from the autocorrelation plots that the core of the *Hinode* data within ±30 s delay time, which is sampled with three data points, is now well resolved with the aid of the SST data. Also, at shorter times, c takes a cusp-like profile. Extrapolating this to delay times of the order of 1 s, we expect to see a steep increase in the rms velocities[7] of the BP motions. The bottom left panel shows the cross-correlation as a function of delay time. The SST data show a small but a consistent and overall negative c_{xy} while the *Hinode* data show a small positive correlation. We suggest that the real cross-correlation $c_{xy} \approx 0$ and the measured values are due to a small number of measurements with high velocities (largely exceeding the rms values). The lower right panel of Figure 6 shows the number of measurements N_n used in the correlation analysis for both the SST and *Hinode* data. To obtain good statistics we collected enough BP measurements to ensure that $N_n \gtrsim 500$ for all bins.

In the rest of the section, we describe the method of estimating the errors in the velocity measurements due to positional uncertainties by analyzing $c(t)$. Following Nisenson et al. (2003), we assume that the errors in the positions are uncorrelated from frame to frame and randomly distributed with a

[7] The correlation at zero-time lag is the variance of the velocity distribution.

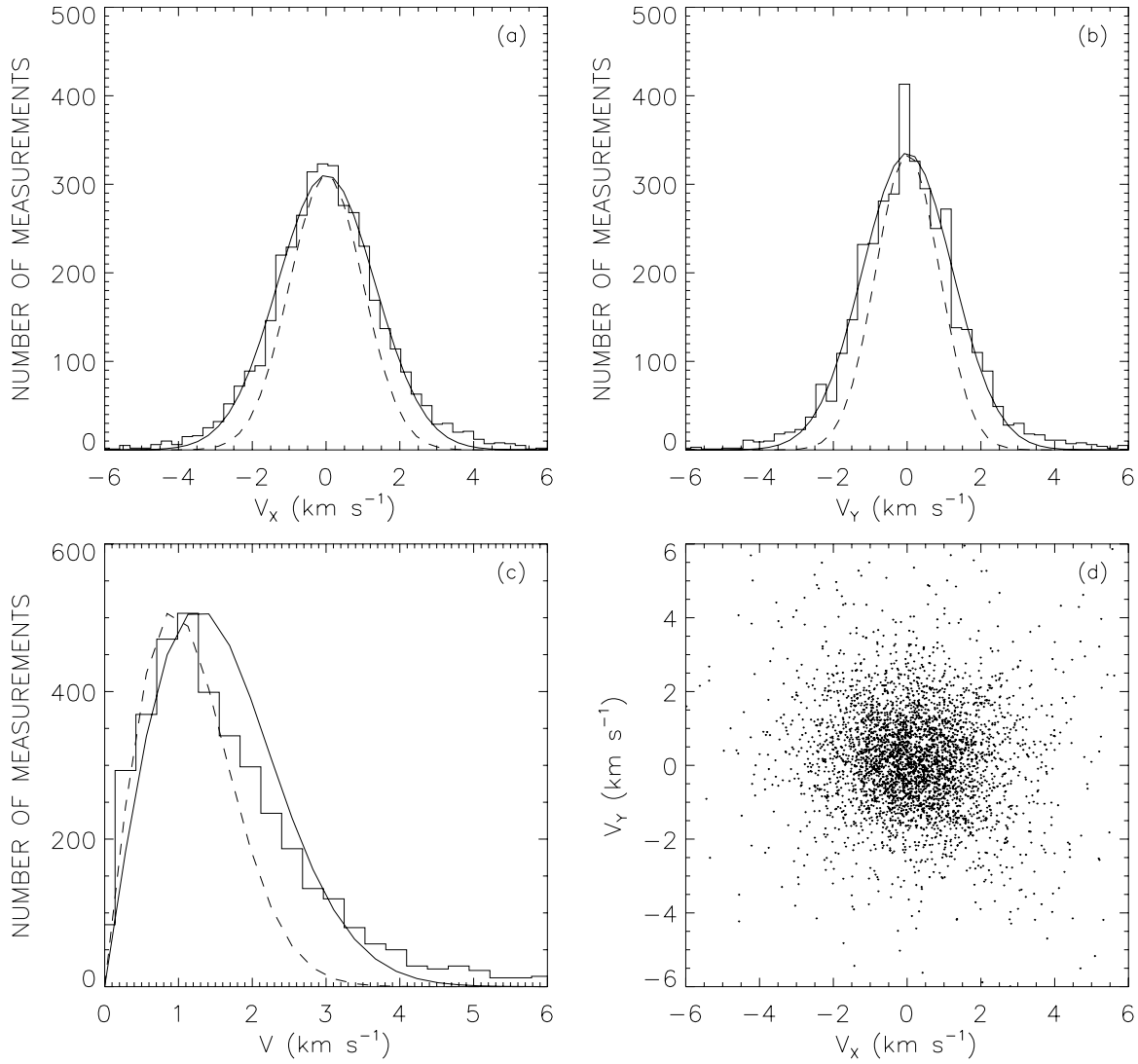

Figure 5. Histograms of measured BP velocities: (a) v_x, (b) v_x, (c) $v = \sqrt{v_x^2 + v_y^2}$. Solid Gaussians in the top panels are fits to the histograms. Dashed Gaussians in panels (a) and (b), and dashed Rayleigh profile in panel (c), are the new distributions of velocities after correcting for the measurement errors (see the text for details); panel (d) shows v_x plotted against v_y.

standard deviation of σ_p. Since the velocities are computed by taking simple differences between position measurements (see above), the measurement errors increase the observed velocity correlation at $n = 0$ by Δ (error), and reduce the correlations at $n = \pm 1$ by $-\Delta/2$, where $\Delta = 2(\sigma_p/\delta t)^2$ and δt is the cadence (see Equation (3) in their paper). We define

$$\Delta_n = \begin{cases} \Delta & \text{when } n = 0 \\ -\frac{1}{2}\Delta & \text{when } n = \pm 1 \\ 0 & \text{otherwise,} \end{cases} \tag{7}$$

which is valid only with our two-point formula for the velocity. Once Δ is determined, the rms values ($\sigma_{v,c}$) of the true solar velocities can be measured as $\sigma_{v,c}^2 = \sigma_{v,r}^2 - \Delta$.

A previous study using data from the Swedish Vacuum Solar Telescope (van Ballegooijen et al. 1998) assumed $c(t)$ to be a Lorentzian. Here, we clearly see that $c(t)$ differs from a Lorentzian, and it can be fitted with a function $\mathfrak{C}$, which is a sum of the true correlation of solar origin ($\mathfrak{C}'$) and Δ, given by

$$\mathfrak{C}_n(\Delta, \tau, \kappa) = \mathfrak{C}'_n(\tau, \kappa) + \Delta_n, \tag{8}$$

where

$$\mathfrak{C}'_n(\tau, \kappa) = a + \frac{b}{1 + \left(\frac{|t_n|}{\tau}\right)^{\kappa}} \tag{9}$$

is a generalized Lorentzian. Δ, τ (correlation time), and κ (exponent) are the free parameters of the fit; a and b are the functions of (Δ, τ, κ), which are determined analytically by least-squares minimization (see the Appendix). We also bring to the notice of the reader that our formula for $\mathfrak{C}$ is a monotonically decreasing function of t_n. However, there is an unexplained increase in the observed c_{yy} beyond ± 100 s (panel (b) in Figure 6). To eliminate any spurious results due to this anomaly, we use a maximum delay time of ± 105 s to fit c with $\mathfrak{C}$ by minimizing the sum of the squares of their difference, as defined in Equation (A1).

The top panel in Figure 7 shows the results listing the best-fit values of the free parameters (Δ, τ, κ), a, and b for a maximum t_n of ± 105 s. $\mathfrak{C}$ (black) and $\mathfrak{C}'$ (thin red) are plotted as functions of the delay time over $c_{xx,n}$ (left, symbols) and $c_{yy,n}$ (right, symbols). The value of Δ where χ^2 has its global minimum is found to be 0.75 km^2 s^{-2}, for both c_{xx} and c_{yy}. The bottom

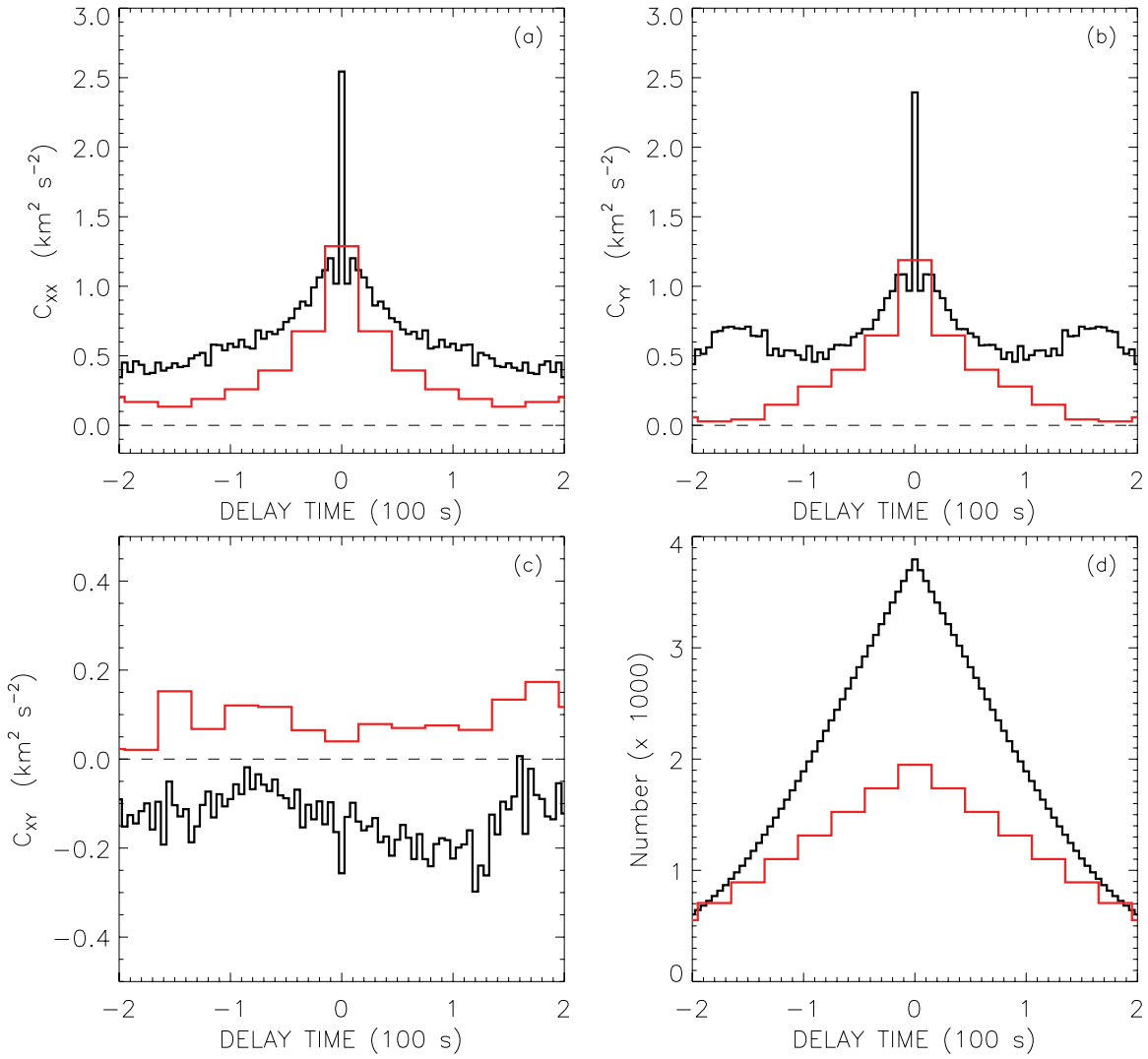

Figure 6. Correlation functions of BP velocities v_x and v_y. (a) Observed autocorrelation $c_{xx,n}$ as a function of delay time t (black: SST; red: *Hinode*). (b) Similar for the observed autocorrelation $c_{yy,n}$. (c) Cross-correlation $c_{xy,n}$ as function of delay time. (d) Number of measurements per bin used in panels (a), (b), and (c).
(A color version of this figure is available in the online journal.)

panel shows the contours of χ^2 as a function of τ and κ at $\Delta = 0.75$ km^2 s^{-2}, and the min(χ^2) is denoted by plus symbols. Dashed and solid lines are the regions of 1.5 and 2 times the min(χ^2), respectively. χ^2 is a well-bounded function for $\kappa < 2$, confirming a cusp-like profile. The correlation time is 22–30 s, which is about 4–6 times the time cadence.

Taking into account the variance in errors (i.e., $\Delta = 0.75$ km^2 s^{-2}), we get $\sigma_p = 3$ km, and the corrected rms velocities ($\sigma_{v,c}$) of v_x and v_y are now 1.00 and 0.86 km s^{-1}. These results are plotted as dashed curves in panels (a) and (b) of Figure 5, and the values are tabulated in the last row of Table 1. The corrected distribution of v is shown as a dashed Rayleigh distribution in panel (c). With higher cadence observations, these results can be refined and modified, as (Δ, τ, κ) depend on the shape of the core of c. By comparing the SST and *Hinode* results, we expect that the observed c probably increases rapidly below 5 s and thus changing the set of parameters to some extent.

5. SUMMARY AND DISCUSSION

We studied the proper motions of the BPs using wideband Hα observations from the SST and the *G*-band data from *Hinode*. BPs were manually selected and tracked using $5'' \times 5''$ areas surrounding them as reference frames. The quality of the SST observations allowed us to measure the BP positions to a sub-pixel accuracy with an uncertainty of only 3 km, which is at least seven times better than the value reported by (Nisenson et al. 2003), and comparable to the rms value of 2.7 km due to image jittering reported by Abramenko et al. (2011). They adopted this rms value of 2.7 km as a typical error of calculations of the BP position. We found that the horizontal motions of the BPs in x and y are Gaussian distributions with *raw* (including the true signal and measurement errors) rms velocities of 1.32 and 1.22 km s^{-1}, symmetric in v-space, observed at 5 s cadence. The above estimate of the measurement uncertainty is obtained from a detailed analysis of the velocity autocorrelation functions. For this, we fitted the observed $c(t)$ with $\mathfrak{C}$, a function of the form shown in Equation (8), and estimated an rms error of about 0.87 km s^{-1} in v_x and v_y. The removal of this error makes the v_x and v_y Gaussians narrower with new standard deviations 1.00 and 0.86 km s^{-1} (a fractional change of 30%). The total rms velocity (v_x and v_y combined) is 1.32 km s^{-1}. The correlation time is found to be in the range of 22–30 s.

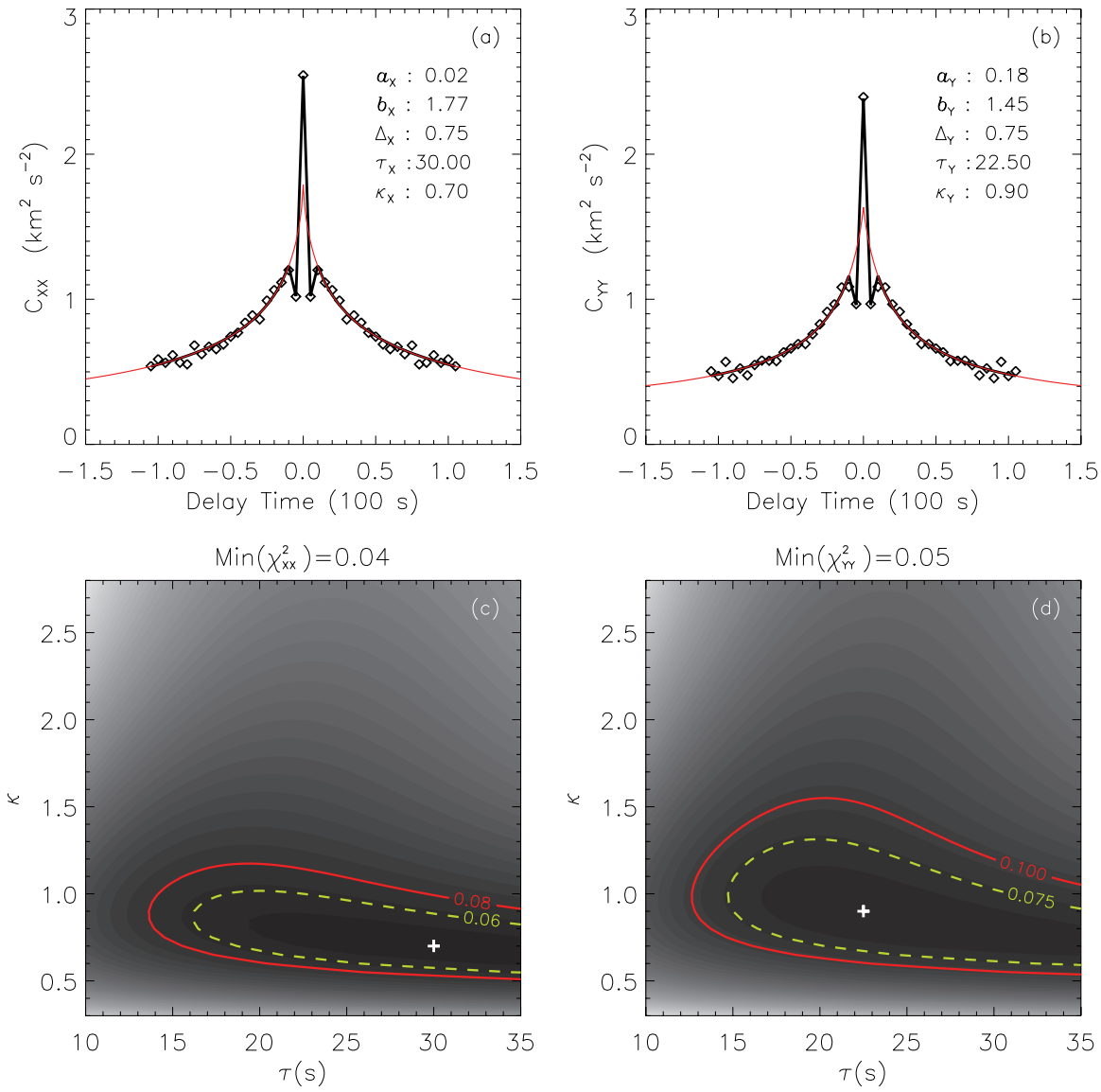

Figure 7. Top: $\mathfrak{C}$ (black curve) plotted as a function of delay time with the best-fit values of a, b, Δ, τ, and κ obtained by minimizing the χ^2 (see the Appendix) of the observed c (shown as symbols, c_{xx}: left; and c_{yy}: right, also shown as black curves in the top panels of Figure 6), and the modeled correlation function $\mathfrak{C}$, for a delay time of ± 105 s in steps of 5 s. Thin red curve is the profile of $\mathfrak{C}'$. Bottom: contour plots of χ^2 as a function of κ and τ, for a value of Δ ($\Delta_x = \Delta_y = 0.75$ km^2 s^{-2}), where χ^2 attains the global minimum. Plus symbol is the global minimum of χ^2; dashed and solid lines are the contours of 1.5 min(χ^2) and 2 min(χ^2), respectively. (A color version of this figure is available in the online journal.)

Following is a brief note and discussion on the additional results we derive from our work. BPs are advected by the photospheric flows. Thus, taking these features as tracers, we can derive the diffusion parameters of the plasma. As BPs usually have lifetimes of the order of minutes, the motion of these features can be used to study the nature of photospheric diffusion at short timescales. The mean-squared displacement of BPs $\langle(\Delta r)^2\rangle$ as a function of time is a measure of diffusion. It is suggested in the literature that $\langle(\Delta r)^2\rangle$ can be approximated as a power law with index γ (i.e., $\langle(\Delta r)^2\rangle \sim t^{\gamma}$; see, for example, Cadavid et al. 1999; Abramenko et al. 2011). In Figure 8, we plot the observed $\langle(\Delta r)^2\rangle$ (symbols) for the 200 s interval on a log–log scale. Solid line is the least-squares fit with a slope of 1.59, which is consistent with the value $\gamma = 1.53$ found by Abramenko et al. (2011) for quiet Sun. Despite the differences in the observations (instruments and observed wavelengths), and analysis methods (identification and tracking of BPs), a close agreement in the independently estimated γ suggests that this is a real solar signal. Both these results assert the presence of super-diffusion (i.e., $\gamma > 1$) for time intervals less than 300 s. Since most of the BPs in this study are tracked for only 3–4 minutes, we cannot comment on the diffusion at longer times.

Note that there is a general relationship between the mean-squared displacement $\langle(\Delta r)^2\rangle$ and the velocity autocorrelation function $\mathfrak{C}'$,

$$\langle(\Delta r)^2\rangle = \left\langle \left(\int_0^t v_x(t')dt' \right)^2 \right\rangle + \left\langle \left(\int_0^t v_y(t')dt' \right)^2 \right\rangle \quad (10)$$

$$= 2 \int_0^t \int_0^t \mathfrak{C}'(t'' - t')dt'dt'', \quad (11)$$

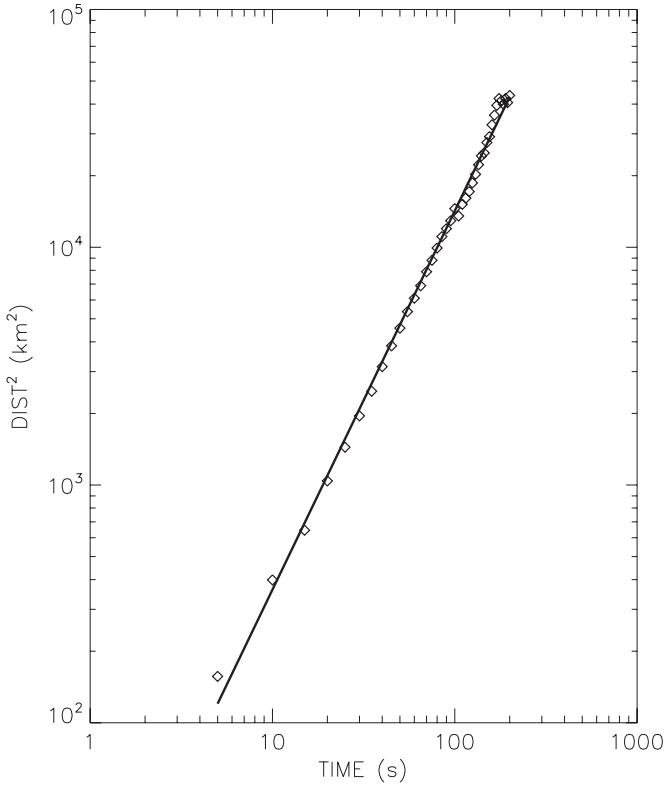

Figure 8. Mean-squared displacement $\langle(\Delta r)^2\rangle$ as a function of time t on a log–log scale. Solid line is the least-squares fit of the observations (symbols), with a slope of 1.59.

where we assume isotropy of the BP motions ($\mathfrak{C}'_{xx} = \mathfrak{C}'_{yy} = \mathfrak{C}'$). For a known autocorrelation or mean-squared displacement, the other quantity can be derived using the above relation.

We already saw that the horizontal motions of the BPs yield several important properties of the lower solar atmosphere. One more such important property is the possibility of the generation of Alfvén waves due to these motions. Here we qualitatively estimate and compare the power spectrum of horizontal motions as a function of frequency for two forms of the velocity correlation function[8]: (a) the form $\mathfrak{C}'$ (Equation (9)), obtained in this study, and (b) a Lorentzian function. For case (a) we use $a = 0$, and also assume that $\mathfrak{C}'_{xx,n} = \mathfrak{C}'_{yy,n}$, with the parameters b, τ, and κ taking the mean values of x and y. For case (b) we use a modified form of $\mathfrak{C}'$ with $\kappa = 2$. The other parameters (a, b, and τ) are the same as in case (a). Figure 9 shows the power spectra for the two described cases: (a) solid line and (b) dashed line. We observe that for frequencies exceeding 0.02 Hz (<50 s), the horizontal motions generally have more power in case (a) as compared to case (b). This highlights the fact that the dynamics of the BPs at short timescales are very important. Therefore, it is highly desirable to do these observations and calculations at very high cadence.

The measurements presented in this paper provide important constraints of models for Alfvén and kink wave generation in solar magnetic flux tubes. As discussed in the Introduction, such waves may play an important role in chromospheric and coronal heating. In the Alfvén wave turbulence model (van Ballegooijen et al. 2011; Asgari-Targhi & van Ballegooijen 2012), it was

[8] Fourier transform of the velocity autocorrelation is the power spectrum.

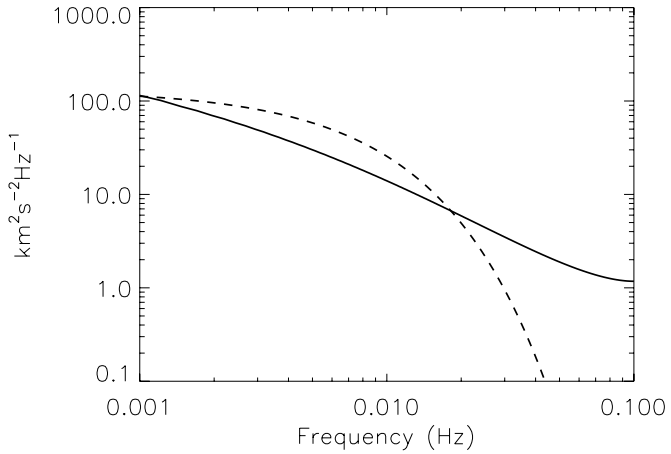

Figure 9. Power spectrum of the horizontal motions (due to v_x) of BPs as a function of frequency derived from autocorrelation function for two cases. Solid line: case (a)—from this study. Dashed line: case (b)—from a Lorentz profile with same a, b, and τ as in case (a) but with $\kappa = 2$ (see the text for details).

assumed that the photospheric footpoints of the magnetic field lines are moved about with rms velocity of 1.5 km s^{-1}, similar to the rms velocity of 1.32 km s^{-1} found here. However, the models include only the internal motions of a flux tube, whereas the observations refer to the displacements of the flux tube as a whole. Clearly, to make more direct comparisons between models and observations will require imaging with high spatial resolution (<0.1 arcsec). This may be possible in the future with the Advanced Technology Solar Telescope.

In this work we presented the results of the BP motions, some of their implications, and use in the context of photospheric diffusion and coronal wave heating mechanisms. We interpret the location of the intensity maximum of a BP as its position at any given time. This is certainly plausible for time periods when we begin to see the physical motion of a BP as a *rigid body* due to the action of the convection on the flux tubes. But at timescales shorter than one minute, other interpretations are also plausible: the motions marked by the intensity maxima could be intensity fluctuations in an otherwise static BP. Nevertheless, these fluctuations are manifestations of some disturbances inside the BP, which are equally important and interesting to explore further.

The authors thank the referee for many comments and suggestions that helped improve the presentation of the manuscript. L.P.C. is a 2011–2012 SAO Pre-Doctoral Fellow at the Harvard-Smithsonian Center for Astrophysics. The Swedish 1 m Solar Telescope is operated on the island of La Palma by the Institute for Solar Physics of the Royal Swedish Academy of Sciences in the Spanish Observatorio del Roque de los Muchachos of the Instituto de Astrofísica de Canarias. Funding for L.P.C. and E.E.D. is provided by NASA contract NNM07AB07C. *Hinode* is a Japanese mission developed and launched by ISAS/JAXA, collaborating with NAOJ as a domestic partner, NASA and STFC (UK) as international partners. Scientific operation of the *Hinode* mission is conducted by the *Hinode* science team organized at ISAS/JAXA. This team mainly consists of scientists from institutes in the partner countries. Support for the post-launch operation is provided by JAXA and NAOJ (Japan), STFC (UK), NASA (USA), ESA, and NSC (Norway). This research has made use of NASA's Astrophysics Data System.

APPENDIX

DETERMINATION OF a AND b

In this section, we briefly describe a method of determining a and b for a set of parameters (Δ, τ, κ). We define the χ^2 of the autocorrelation functions of v_x and v_y as

$$\chi^2_{xx}(\Delta, \tau, \kappa) = \sum_{n=-N}^{N} [c_{xx,n} - \mathfrak{C}_n(\Delta, \tau, \kappa)]^2, \text{ and}$$

$$\chi^2_{yy}(\Delta, \tau, \kappa) = \sum_{n=-N}^{N} [c_{yy,n} - \mathfrak{C}_n(\Delta, \tau, \kappa)]^2, \quad \text{(A1)}$$

where $c_{xx,n}$ and $c_{yy,n}$ are the observed autocorrelation values of velocities v_x and v_y, and $\mathfrak{C}$ is a model of the correlation function given by Equation (8). By minimizing the χ^2 with respect to a and b (i.e., $\frac{\partial \chi^2}{\partial a} = 0$ and $\frac{\partial \chi^2}{\partial b} = 0$, separately for x and y), and solving the resulting system of linear equations, we have

$$a = \frac{1}{\alpha\beta' - \alpha'\beta}(\beta' A - \beta B) \quad \text{(A2)}$$

$$b = \frac{1}{\alpha\beta' - \alpha'\beta}(\alpha B - \alpha' A), \quad \text{(A3)}$$

where

$$\alpha = 2n + 1$$

$$\beta = \sum_{n=-N}^{N} \frac{1}{1 + \left(\frac{|t_n|}{\tau}\right)^{\kappa}}$$

$$\alpha' = \beta$$

$$\beta' = \sum_{n=-N}^{N} \frac{1}{\left[1 + \left(\frac{|t_n|}{\tau}\right)^{\kappa}\right]^2}$$

$$A = \sum_{n=-N}^{N} c_n$$

$$B = \sum_{n=-N}^{N} \left(\frac{c_n - \Delta_n}{1 + \left(\frac{|t_n|}{\tau}\right)^{\kappa}} \right).$$

REFERENCES

Abramenko, V. I., Carbone, V., Yurchyshyn, V., et al. 2011, ApJ, 743, 133
Asgari-Targhi, M., & van Ballegooijen, A. A. 2012, ApJ, 746, 81
Berger, T. E., Loefdahl, M. G., Shine, R. S., & Title, A. M. 1998, ApJ, 495, 973
Berger, T. E., Schrijver, C. J., Shine, R. A., et al. 1995, ApJ, 454, 531
Berger, T. E., & Title, A. M. 1996, ApJ, 463, 365
Cadavid, A. C., Lawrence, J. K., & Ruzmaikin, A. A. 1999, ApJ, 521, 844
Chapman, G. A., & Sheeley, N. R., Jr. 1968, Sol. Phys., 5, 442
De Pontieu, B., Hansteen, V. H., Rouppe van der Voort, L., van Noort, M., & Carlsson, M. 2007a, ApJ, 655, 624
De Pontieu, B., McIntosh, S. W., Carlsson, M., et al. 2007b, Science, 318, 1574
de Wijn, A. G., Stenflo, J. O., Solanki, S. K., & Tsuneta, S. 2009, Space Sci. Rev., 144, 275
Jess, D. B., Mathioudakis, M., Erdélyi, R., et al. 2009, Science, 323, 1582
Kosugi, T., Matsuzaki, K., Sakao, T., et al. 2007, Sol. Phys., 243, 3
Manso Sainz, R., Martínez González, M. J., & Asensio Ramos, A. 2011, A&A, 531, L9
McIntosh, S. W., de Pontieu, B., Carlsson, M., et al. 2011, Nature, 475, 477
Muller, R. 1983, Sol. Phys., 85, 113
Muller, R. 1985, Sol. Phys., 100, 237
Muller, R., Roudier, T., Vigneau, J., & Auffret, H. 1994, A&A, 283, 232
Nisenson, P., van Ballegooijen, A. A., de Wijn, A. G., & Sütterlin, P. 2003, ApJ, 587, 458
Scharmer, G. B., Bjelksjo, K., Korhonen, T. K., Lindberg, B., & Petterson, B. 2003a, Proc. SPIE, 4853, 341
Scharmer, G. B., Dettori, P. M., Lofdahl, M. G., & Shand, M. 2003b, Proc. SPIE, 4853, 370
Spruit, H. C. 1981, A&A, 98, 155
Stenflo, J. O. 1973, Sol. Phys., 32, 41
Stenflo, J. O., & Harvey, J. W. 1985, Sol. Phys., 95, 99
Title, A. M., & Rosenberg, W. J. 1981, Opt. Eng., 20, 815
Title, A. M., Tarbell, T. D., & Topka, K. P. 1987, ApJ, 317, 892
Tsuneta, S., Ichimoto, K., Katsukawa, Y., et al. 2008, Sol. Phys., 249, 167
Utz, D., Hanslmeier, A., Muller, R., et al. 2010, A&A, 511, A39
van Ballegooijen, A. A., Asgari-Targhi, M., Cranmer, S. R., & DeLuca, E. E. 2011, ApJ, 736, 3
van Ballegooijen, A. A., Nisenson, P., Noyes, R. W., et al. 1998, ApJ, 509, 435
van Noort, M., Rouppe van der Voort, L., & Löfdahl, M. G. 2005, Sol. Phys., 228, 191